Chemical Engineering Journal xxx (xxxx) xxx

Contents lists available at ScienceDirect

Chemical Engineering Journal

journal homepage: www.elsevier.com/locate/cej

CO_2 solubility in brine in silica nanopores in relation to geological CO_2 sequestration in tight formations: Effect of salinity and pH

Wenhui Li [a], Yiling Nan [a], Qing You [b,*], Zhehui Jin [a,*]

[a] School of Mining and Petroleum Engineering, Department of Civil and Environmental Engineering, University of Alberta, Edmonton, AB T6G 1H9, Canada
[b] School of Energy Resources, China University of Geosciences, Beijing 100083, China

ARTICLE INFO

Keywords:
Salinity
pH
CO_2 solubility
Tight formation
Molecular dynamics simulation

ABSTRACT

Geological CO_2 sequestration during CO_2 enhanced oil recovery in tight formations is a technically and economically viable option to alleviate carbon emission. In tight formations, there existsare enormous number of nano-scale pores, which can be filled with connate and injected water. In addition, the salinity and pH of the formation water vary regionally. In this work, we used molecular dynamics simulations to study the effects of salinity and pH on CO_2 solubility in brine in silica nanopores under typical geological conditions (353 K and ~ 175 bar). The pH effect is characterized by the deprotonation degree of silanol on the silica surface. We find that water mainly distributes around the silanol groups and CO_2 mainly enriches in the areas where silanol groups are vacant. Na^+ ions are generally depleted from the non-deprotonated silica surface, whereas they are strongly attracted to the pore surfaces in the deprotonated cases. The different water hydration structures around the non-deprotonated and deprotonated silanols arise from the accumulation of Na^+ ions in the vicinity of $\equiv SiO^-$ groups. As salinity increases, the average densities of CO_2 and water decrease in all silica nanopores and CO_2 solubility in brine in silica nanopores decreases. On the other hand, as pH increases, water density increases but CO_2 density decreases, resulting in a decrease of CO_2 solubility in brine in silica nanopores. CO_2 solubility in brine with a low pH range (~2–5) can be as high as 1.3–1.6 times of that in bulk, while it is comparable with that in bulk at a high pH range (~7–9). Overall, low salinity and low pH conditions are favored for geological CO_2 sequestration by solubility trapping in tight formations.

1. Introduction

Carbon capture and storage (CCS) has been broadly recognized as a viable method to mitigate the carbon emissions due to the continuous consumption of fossil fuels [1]. Long-term storage of carbon dioxide (CO_2) is the last step for the CCS chain [2]. Among all the storage methods, geological CO_2 sequestration has been proven to be technically and economically viable [2–5]. According to the Global Status of CCS (2019) [6], there are 19 industrial level CCS facilities in operation globally. These projects can capture and permanently store ~37 million tonne (Mt) of CO_2 annually, among which ~30 Mt are stored in the form of CO_2 enhanced oil recovery (EOR) which can effectively offset the financial burdens associated with the geological CO_2 sequestration [1]. On the other hand, according to the Annual Energy Outlook (2019) [7] by US Energy Information Administration, tight oil (oil deposited in tight formations) is an important US energy supply, accounting for 61% of total US oil production in 2018, while its production continues to increase through 2030. One of the most promising methods to recover tight oil is CO_2-EOR, which has been successfully implemented in many tight oil fields accompanied with CO_2 sequestration [8–10]. Therefore, CO_2-EOR accompanied with CO_2 sequestration in tight formations becomes environmentally and economically attractive to energy producers and policy makers.

One of the widely used CO_2-EOR methods for tight formations is water alternating gas (WAG) flooding, in which massive amount of water is injected into the formations [9,11]. In addition, the formations usually contain a large amount of connate water originally [12–14]. In tight formations, there exists a considerable number of nanoscale pores, which is comparable to fluid molecular size [15,16], while silica is one of the most common minerals [3,4], which is generally hydrophilic [17]. Therefore, silica nanopores in tight formations can be saturated with the formation water during CO_2-EOR and CO_2 sequestration processes. As the CO_2 dissolution in brine at high pressures underground is one of CO_2 trapping mechanisms in geological CO_2 sequestration, it is imperative to

* Corresponding authors.
E-mail addresses: youqing@cugb.edu.cn (Q. You), zhehui2@ualberta.ca (Z. Jin).

https://doi.org/10.1016/j.cej.2020.127626
Received 12 September 2020; Received in revised form 21 October 2020; Accepted 30 October 2020
Available online 5 November 2020

study CO_2 solubility in brine in silica nanopores.

Several studies have shown that gas solubility in solvent in nanopores is either enhanced or suppressed compared to that in bulk [18–38], which depends on the substrate properties, pore size, molecular configurations of gas and solvent, and the ratio of molecular size between gas and solvent, etc. [26,30,34,36–38]. The detailed review of the previous works can be found in our recent work [37]. Under nano-confinement, gas and solvent molecules can form completely different solvation structures and distributions from those in bulk [26,30,36]. Botan *et al.* reported that CO_2 solubility in water in montmorillonite clay interlayers can be one order of magnitude larger than that in bulk [24]. Our recent study indicated that, in kaolinite nanopores, the kaolinite substrate wettability has a dominant effect on the distributions of CO_2 and water [37]. CO_2 molecules form a strong adsorption layer on the silica facet of kaolinite, enhancing its solubility in water in kaolinite with the silica facet substrates. On the other hand, CO_2 is generally depleted from the gibbsite facet of kaolinite, thus rendering a reduced solubility in water in kaolinite with the gibbsite facet substrates [37]. In addition to the nano-confinement effect, salt ions, which are omnipresent in the formation water, can also play an important role on CO_2 solubility in brine [39–41]. Generally, CO_2 solubility in brine decreases as salinity increases due to the so-called "salting out" effect [39–42]. However, under nano-confinement, the hydration structure of salt ions is altered by the presence of substrates and fluid–solid interactions [34,43]. Therefore, the combined effect of nano-confinement and salt ions on CO_2 and water distributions as well as CO_2 solubility in brine in silica nanopores is imperative to geological CO_2 sequestration in tight formations.

On the other hand, the pH value of an aquifer varies regionally, imposing varying influences on the substrate surface chemistry [17,44,45]. For example, silica as one of the major constituents in tight formations [3,4], has varying surface chemistries as the pH of the formation water varies [17,44–47]. All silanol groups (≡SiOH) on the silica surface are subject to deprotonation-protonation equilibria [17,44,45]. The neutral silanol terminated silica surface can be found at a pH between 2 and 5 [17,44,45]. As pH increases, part of silanol groups are gradually deprotonated. The deprotonation degree can reach up to 20%, when the pH is between 7 and 9 [44,45]. As a result, the pH of the formation water can dictate silica surface chemistry, which varies from a neutrally-charged surface to a negatively-charged one [17,44,45]. Such surface chemistry alteration can further influence CO_2, water, and salt ion distributions. Prior works studied water structures and diffusion in silica nanopores as a function of surface charge [46,47]. These works show that water orientation close to the silica surface is altered, and its diffusion coefficient in silica nanopores is reduced [46,47]. Bonnaud *et al.* [48] investigated Ca^{2+} ion solvation in charged silica nanopores. They found that most Ca^{2+} ions are attracted to the silica surface, while their hydration structure close to the surface is different from that in bulk. Renou *et al.* [49] studied water structural and dynamic properties in three different silica nanopores (protonated surface, deprotonated surface with charge re-distribution, and deprotonated surface with Na^+ charge compensation). They found that the water distribution and diffusion are greatly affected by surface chemistry. Haria and Lorenz [50,51] studied NaCl and $CaCl_2$ solution flow through the charged silica nanopores, in which the effect of pore size, cation type, and salinity were considered. They observed that pore size imposes varying influences on the current of NaCl and $CaCl_2$ solutions as charge inversion was observed in the $CaCl_2$ system which does not occur in the NaCl system. However, to the best of our knowledge, the pH effect on CO_2, water, and salt ion distributions as well as CO_2 solubility in brine in silica nanopores under the geological CO_2 sequestration condition are still not clear.

In this work, we study the coordinated effect of salinity and pH on CO_2 and water distributions in silica nanopores by molecular dynamics (MD) simulations. MD simulation is a computer simulation method for analyzing the physical movements of atoms and molecules by explicitly considering the intermolecular interactions. The trajectories of atoms and molecules are determined by solving the Newton's equations of motion, and further analyzed to obtain structural and thermodynamic properties. Therefore, MD simulation is a powerful tool to explore the microscopic phenomena and mechanisms, especially for the scale and conditions where experiments are hardly accessible (e.g., the high-pressure and high-temperature geological conditions as well as the nanoscale confinement) [52]. Na^+ and Cl^- are used to represent salt ions and six salt concentrations up to ~12 wt% are used to study the salinity effect. Three deprotonation degrees (0%, 8.3%, and 16.7%) of silanol groups are devised to denote the effect of pH. Temperature and pressure are set as 353 K and ~ 175 bar, respectively, which are the typical geological conditions for CO_2 sequestration [3,4].

The remainder of this paper is organized as following. In **Section 2**, the simulation methodology including simulation system, molecular models and validation, and simulation details is presented. In **Section 3**, the salinity and pH effects on the fluid distributions are analyzed by presenting the density distributions normal to the pore surface, 2-D density contour plot parallel to the pore surface, and the radial density distributions around the silanol and siloxide groups on the pore surface. Then, we present the effect of salinity and pH on CO_2 solubility in brine in silica nanopores. In **Section 4**, the key findings and potential implications are summarized.

2. Simulation methodology

2.1. Simulation system

An example of simulation systems is depicted as Fig. 1**(a)**. The center of the simulation system is brine confined in a silica slit nanopore with a length of ~12 nm in the *x*-direction. On both sides of the pore, two ~6 nm brine slabs and two ~6 nm CO_2 slabs are placed symmetrically. The brine and CO_2 slabs serve as the outside bulk brine reservoirs and bulk CO_2 phase, respectively. CO_2 and water molecules as well as salt ions can freely move within the system via molecular diffusion. Once the system reaches equilibrium, the fluid distributions in the nanopore and bulk can be obtained in the corresponding regions. The salt ions are Na^+ and Cl^-, which are the most common ions in brine [39–41]. The salinities in the outside bulk brine reservoirs range from 0 to ~12 wt%, which covers the typical salinity range of formation water underground [39–41]. The initial setting for each system can be found in **Table S1** in the **Supporting Information** (**SI**).

The silica nanopores consist of two identical amorphous silica sheets with hydroxylated inner surface. Amorphous silica is chosen because it is one of the most abundant constituents in tight sandstone formations [3,4]. The amorphous silica is constructed based on Emami *et al.* [44]. The surface area of the silica sheet is ~12 × 8.3 nm^2 (the *x*-*y* plane), and the thickness of each silica sheet is around 1.5 nm. The roughness of the inner surface is illustrated in Fig. 1**(b)**. The amplitude, namely, the vertical deviation from the mean line, is around 0.03 nm. The silica slab consists of 3 × 2 periodic cells in the *x*- and *y*-directions as shown in Fig. 1**(c1)**−**(c3)**, where the blue and green solid circles are Si atoms in ≡SiOH and in ≡SiO^-, respectively. ≡SiO^- groups in Fig. 1**(c2)** and **(c3)** are randomly picked and converted from ≡SiOH groups in Fig. 1**(c1)**, which account for 8.3% and 16.7% of the total number of surface groups, respectively. These three configurations of silica surface correspond to the pH values of ~2–5, ~5–7, and ~7–9, respectively [17,44,45], which cover the typical pH ranges in tight formations [53,54]. While the dissolved CO_2 in brine is subject to the reaction with water to form carbonic acid, the concentration of H_2CO_3 is three orders of magnitude smaller than the dissolved CO_2 concentration [55]. Therefore, the formation of carbonic acid is not considered in this work. The density of ≡SiOH groups in Fig. 1**(c1)** is 4.74/nm^2, which is in line with the experimental measurements (average at 4.6–4.9/nm^2) [56–58]. The pore size is around 2.5 nm, representing a typical nanopore in tight sandstone formations [15,16].

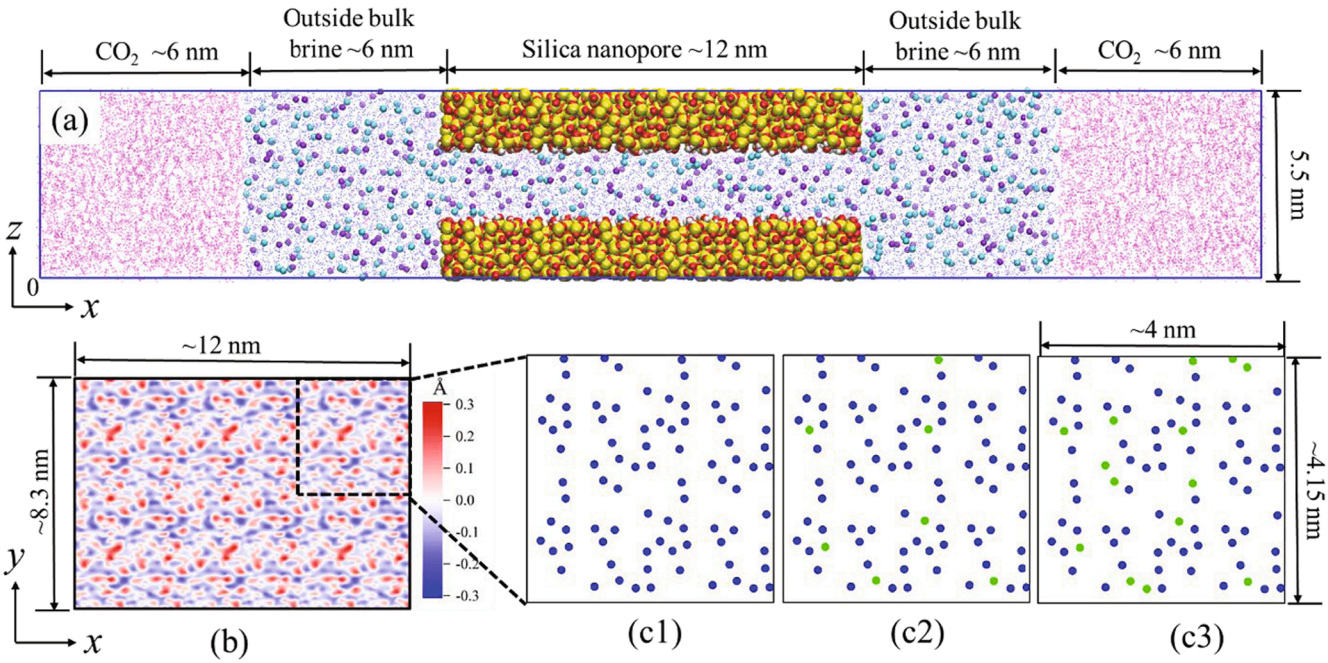

Fig. 1. (a) Schematic representation of simulation system. The yellow, red, white, purple, and cyan spheres represent Si, O, H, Na^+, and Cl^-, respectively; the blue and pink dots are water and CO_2 molecules, respectively. (b) The surface roughness characterization: zero in the legend represent the average position of the surface atoms (excluding H atoms) in the *z*-direction, and the positive and negative values represent the coordinate deviation of surface atoms from the average position. (c1)-(c3) The distribution of Si atoms in the groups of ≡SiOH and ≡SiO^- on the surface of a periodic cell (the surface consists of 3 × 2 periodic cells in the *x*- and *y*-directions); the blue and green circles represent Si atoms in ≡SiOH and in ≡SiO^-, respectively. ≡SiO^- groups in (c1), (c2), and (c3) account for the deprotonation degree of 0.0%, 8.3%, and 16.7%, respectively, which corresponds to pH of ~2–5, ~5–7, and ~7–9, respectively. (For interpretation of the references to colour in this figure legend, the reader is referred to the web version of this article.)

2.2. Molecular models and validation

Silica is described by the parameters from Emami *et al* [44]. Water and CO_2 molecules are modeled by SPC/E [59] and EPM2 [60] models, respectively. Salt ions (Na^+ and Cl^-) parameters are adopted from Smith and Dang (SD) [61]. The force field parameters can be found in **Tables S2 and S3** in the **SI**. The choice of such force field combination is based on the following consideration: First, regarding the silica, the parameters developed by Emami *et al.* resolve numerous limitations of prior silica parameters and reduce the uncertainties in the calculated interfacial properties comparing to experimental data [44]. It explicitly considers the full range of variable surface properties (such as zeta potential and silanol surface density) and pH (silanol deprotonation degree) [44]. It has been proven to accurately predict water contact angles in the water–gas (CO_2 or air)-silica systems [17,44]. Moreover, this silica model is compatible with the commonly used water models (such as SPC series and TIP series) [44]. Second, the water and CO_2 models are carefully chosen among various combinations by comparing simulation results with experimental measurements in terms of CO_2 bulk density [62], CO_2-water interfacial tension (IFT) [63], CO_2 solubility in bulk water [41], and CO_2 diffusion coefficient in bulk water [64] over a broad range of pressure. The results indicate that the optimized SPC/E and EPM2 [65] can quantitatively reproduce the above-mentioned properties and outperform other force field combinations (see the results in **Fig. S1** and the detailed discussion in context in the **SI**). Therefore, the optimized SPC/E and EPM2 are selected to model water and CO_2 molecules. Third, because SPC/E model [59] has been selected for water, the salt ion force field should be compatible with SPC/E water. SD model for NaCl [61] is a widely accepted one to describe brine coupled with SPC/E water [61,66–69]. Finally, we also compare the CO_2 solubility in brine [40] and CO_2-brine IFT [70] to experimental data over a wide range of salinity (see the results in **Fig. S2** and the detailed discussion in context in the **SI**). The semi-quantitative agreement demonstrates that the water, CO_2, and salt ion models can mimic the salinity effect with a reasonable accuracy.

2.3. Simulation details

All simulations are conducted by the GROMACS package (version 2019.5) [71,72]. The systems are first relaxed by the steepest descent algorithm until the maximum force is less than 1000 $kJ{\cdot}mol^{-1}{\cdot}nm^{-1}$. Afterward, a 50-ns *NVT* simulation is conducted for equilibration in each case with a time step of 2 fs. The equilibrium is carefully checked by comparing CO_2, water, and salt ion density distributions in the silica nanopores, CO_2 solubility in the outside bulk brine reservoirs and in the silica nanopores, and CO_2 density in the bulk CO_2 phase every 5-ns in each case (see **Figs. S3 and S4** in the **SI** as an example). We find that these properties stabilize in all cases within this time period, suggesting that the systems are equilibrated in 50 ns. The sampling stage is conducted following the equilibration stage with either 10-ns or 20-ns *NVT* simulations for each case (refer to **Table S1** for details). The trajectory in the sampling stage is saved every 100 steps (200 fs) for analysis. As a result, the ensemble averaged properties are obtained over 50,000 or 100,000 configurations. Three-dimensional periodic boundary conditions (PBCs) are applied. The cut-off distance for Lenard-Jones potential is 1.2 nm and compensated by analytical tail corrections [73]. The long-range Columbic interaction is addressed by the particle-mesh Ewald (PME) algorithm [74]. The silicon and bulk oxygen atoms in the silica substrate are fixed throughout the simulation, whereas the functional groups (hydroxyls and deprotonated hydroxyls) on the silica surface are allowed to rotate around silicon atoms (see **Table S3** in the **SI**). Water and CO_2 molecules are treated as rigid bodies by the SETTLE algorithm [75] and by introducing two virtual atoms [76], respectively. The system pressure (174.5 ± 1.5 bar, see **Table S1** for details) is dictated by CO_2 density in the bulk CO_2 phase from the NIST Chemistry Webbook [62] as the CO_2 model used in this work can accurately reproduce its bulk density in the studied range of pressures (see **Fig. S1(a)** in the **SI**). The system temperature (set as 353 K) is controlled by the velocity-

rescale thermostat [77].

3. Results and discussion

In this section, we first present the 1-D density profiles normal to the silica surface (along the *z*-direction), and then the 2-D density contour plots in the adsorption layer parallel to the silica surface (the *x*-*y* plane) are illustrated. Then, the radial density distributions around the silanol and siloxide groups are presented to show the effect of surface chemistry on fluid distributions. Finally, the CO_2 solubility in brine in silica nanopores and in bulk under various salinities and pH values are calculated.

3.1. Density distributions in the z-direction

In Fig. 2, we present the number density distributions of each element in silica nanopores along the *z*-direction in the non-deprotonated cases with various salinities. The oxygen and hydrogen atoms in water molecules are denoted as Ow and Hw, respectively; the oxygen and carbon atoms in CO_2 molecules are denoted as Oc and Cc, respectively. The data are extracted from the central region of the silica nanopores (from $x = 14$ to 22 nm) to avoid the pore end effect as in our previous work [37]. While the statistical errors in density profiles are not shown in Fig. 2 for clarity, they would be reflected in the solubility calculations (see **Section 3.4**). We also present an example to show the oscillations of each elemental density profile in **Fig. S5**. As seen from Fig. 2, water has a layering structure close to the silica surface, forming two adsorption layers for both Ow and Hw on each surface. In addition, CO_2 also forms a single adsorption peak on each surface, while salt ions are generally depleted from the surface, which is in line with the previous studies [43,46,47]. As salinity increases, the densities of water and CO_2 monotonically drop in both the adsorption layer and bulk region. In **Figs. S6 and S7**, we also depict the number density distributions of each element in the silica nanopores with deprotonation degrees of 8.3% and 16.7%, respectively. As pH increases (the silica surface deprotonation degree increases), the water adsorption layer becomes increasingly prominent, whereas CO_2 adsorption layer gradually weakens. As deprotonation degree increases from 0.0%, Na^+ ion distributions change from the depletion at the pore surface to the enrichment due to the electrostatic interactions, generating several noticeable spikes in density profiles, while Cl^- ions are always depleted from the silica surface. The increase in water density in the vicinity of the pore surfaces as the deprotonation degree increases is probably because as more Na^+ ions are attracted to the pore surfaces, more water molecules are needed to hydrate these counter-ions. Overall, all water, CO_2, and salt ion density distributions converge to their respective bulk values away from the silica surfaces (see **Fig. S8** in the **SI**).

In Fig. 3, we present the number density distributions, reduced density distributions as well as orientation parameters in silica nanopores with deprotonation degree of 0.0% at salinity of 7.33 wt%. The reduced density distributions represent the number density distributions normalized by the density of the corresponding component in the outside brine reservoirs. The orientation parameters S_z of water and CO_2 are given as [37]:

$$S_z = 1.5 \times \langle cos^2\theta_z \rangle - 0.5 \quad (1)$$

where θ_z is the angle between the *z*-axis and molecular axis (the lines connecting two Hw atoms for water and two Oc atoms for CO_2, respectively, as shown in the inset of Fig. 3**(b)**), and $\langle \cdots \rangle$ implies the ensemble average. Positive, zero, and negative orientation parameters represent perpendicular, random, and parallel alignments of molecular axis to the silica surface, respectively. Only the data in the range of 1.5 nm $< x <$ 4.0 nm are presented. Beyond this range, too few water and CO_2 molecules are found therein because of the rough surface. Fig. 3 shows that CO_2 molecules co-adsorb on the silica surface with water, while salt ions are depleted. Regarding the molecular orientation, from the pore surface to the middle of the pore, water molecules are parallel to the pore surface first, then gradually become randomly oriented and followed by a weakly-parallel alignment at its density peak position. On the other hand, CO_2 molecules gradually change from a perpendicular

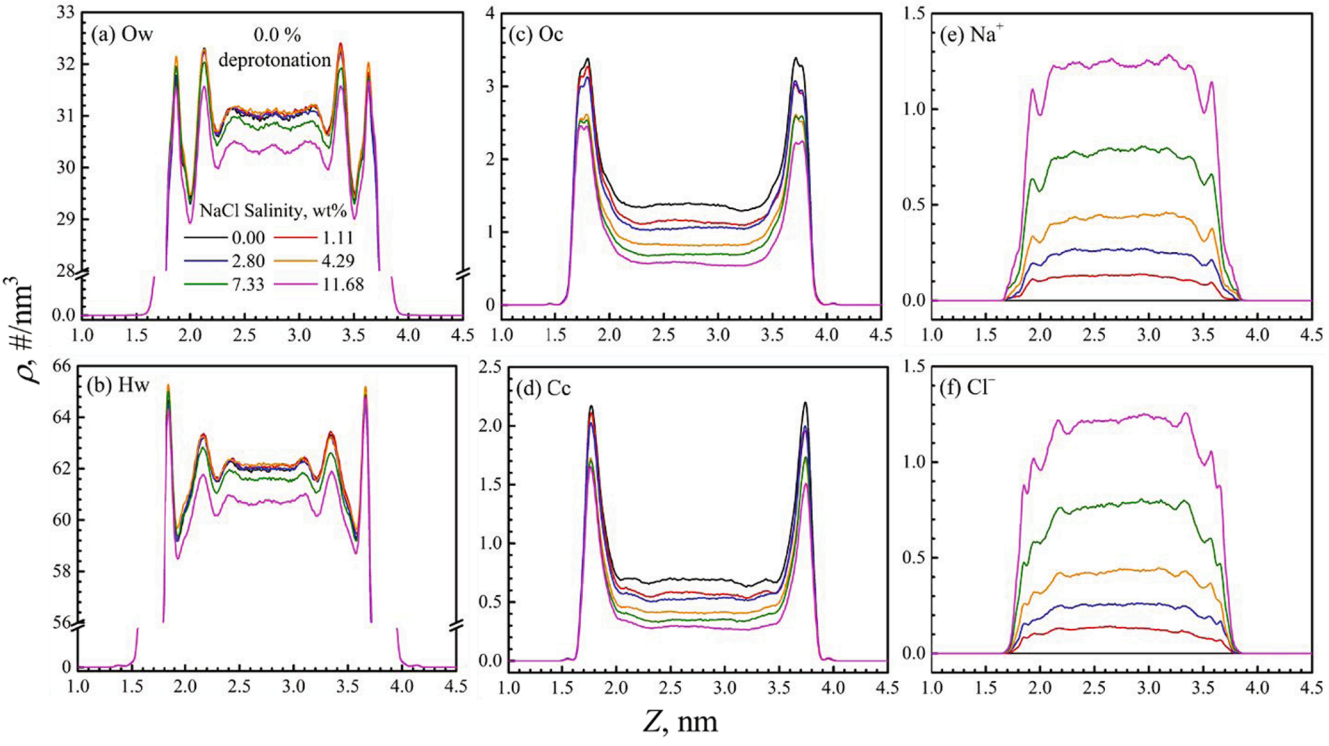

Fig. 2. Number density distributions of each element in silica nanopores in the *z*-direction with a deprotonation degree of 0.0% at various salinities. Ow, Hw, Oc, and Cc represent oxygen and hydrogen atoms of water, oxygen and carbon atoms of CO_2, respectively.

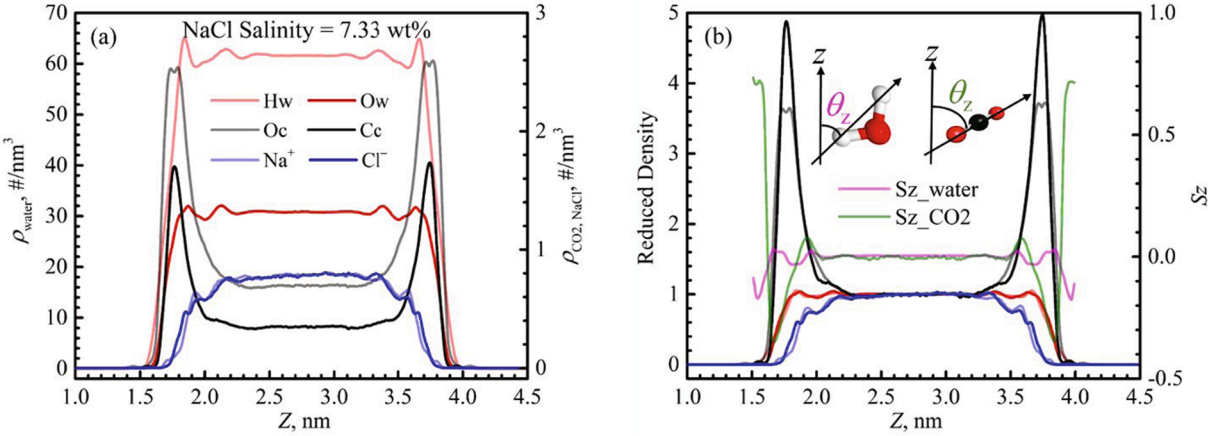

Fig. 3. (a) Number density distributions; (b) reduced density distributions as well as the orientation parameters in silica nanopores at salinity of 7.33 wt% and deprotonation degree of 0.0%. Ow, Hw, Oc, and Cc represent oxygen and hydrogen atoms of water, oxygen and carbon atoms of CO_2, respectively.

alignment at the pore surface to a parallel alignment in the CO_2 adsorption layer. In **Figs. S9 and S10**, we present, respectively, the number density distributions, reduced density distributions as well as orientation parameters in silica nanopores with deprotonation degree of 8.3% at salinity of 7.37 wt% and deprotonation degree of 16.7% at salinity of 7.70 wt%. Unlike the non-deprotonated cases as shown in Fig. 3, water orientation in those deprotonated cases is weakly perpendicular in the vicinity of the pore surface. CO_2 orientations and distributions, however, are similar to those in the non-deprotonated cases. The differences in water orientations indicate that surface charge can alter water structures close to the pore surface in line with prior results [46,47,49]. Meanwhile, as the deprotonation degree increases, due to the more prominent Na^+ ion accumulation close to the pore surface, Cl^- ions can also enrich beyond Na^+ layers, showing a characteristic of electrical double layer (EDL). We also note that salinity has an insignificant effect on water and CO_2 orientations (see **Fig. S11**). The snapshots in **Fig. S12** present the typical configurations of the cases in Figs. 3**, S9 and S10** by VMD [78]. As deprotonation degree increases, more Na^+ ions but fewer CO_2 molecules are found close to the pore surfaces, which is consistent with Figs. 2**, S6, and S7**.

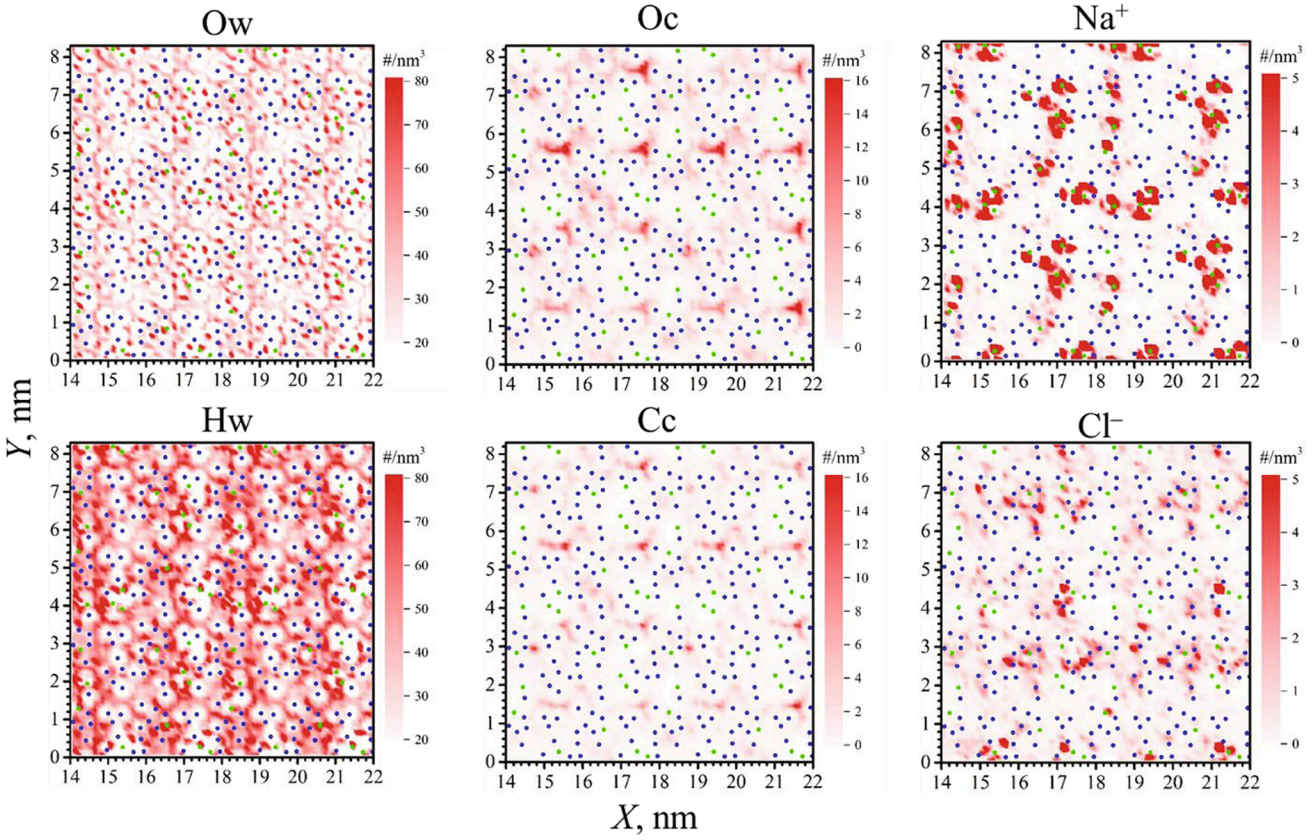

Fig. 4. 2-D density contour plot in the adsorption layer parallel to the pore surface (the *x*-*y* plane) at the salinity of 7.70 wt% and deprotonation degree of 16.7%. Blue and green dots are Si atoms in ≡Si(OH) and in ≡Si(O^-) groups, respectively. Ow, Hw, Oc, and Cc represent oxygen and hydrogen atoms of water, oxygen and carbon atoms of CO_2, respectively. (For interpretation of the references to colour in this figure legend, the reader is referred to the web version of this article.)

3.2. Density distributions in the x-y plane

While the results in Section 3.1 can provide the density distributions of each component along the *z*-direction, they are averaged in the *x-y* plane, which cannot reflect the fluid distributions in the *x-y* plane. Therefore, we present the 2-D density contour plot in the adsorption layer parallel to the pore surface (the *x-y* plane) in Fig. 4 at salinity of 7.70 wt% and deprotonation degree of 16.7%. The adsorption layer for each element is defined as the region from the position where its density is 10% of its bulk density (that in the outside brine reservoirs) to the first local minimum in the *z*-direction.

As shown in Fig. 4, water molecules mainly accumulate around the ≡SiOH and ≡SiO^- groups, whereas CO_2 can only enrich in the areas where these surface groups are scarce. Salt ions, especially Na^+, are strongly attracted by the ≡SiO^- groups owing to the strong electrostatic interaction. However, salt ions are repelled from the ≡SiOH groups. The other cases with deprotonation degrees of 0.0% and 8.3% are depicted in **Figs. S13 and S14**, respectively. As deprotonation degree increases, water density increases, while the opposite is true for CO_2. In addition, Na^+ ions become gradually enriched at the surface. These results are consistent with those in Section 3.1.

3.3. Radial density surrounding the surface groups

To further explore the spatial distributions of water, CO_2 and salt ions around the surface groups (≡SiOH and ≡SiO^-), we present the radial distribution densities of each element around the O atom in ≡SiOH and ≡SiO^- groups in Figs. 5 and 6, respectively. The deprotonation degree is 16.7% and the salinity ranges from 0 to 11.89 wt%. The data are extracted from the central region of the nanopores as well. The radial density is counted as the average number of target elements in the volume of hemi-toroidal shells around the O atom in the surface groups as shown in the schematic insets in Figs. 5(b) and 6(b). The results for the cases with deprotonation degree of 0.0% and 8.3% are shown in **Figs. S15-S17**.

As shown in Figs. 5 and 6, the Ow distributions have a single peak and the Hw distributions have two peaks around the O atom in ≡SiOH groups, while around the O atom in ≡SiO^- groups, both Ow and Hw distributions have a significant density peak at the contact distances followed by a few small oscillations. Besides, CO_2 distribution has a peak around the ≡SiOH groups, while depleted from the ≡SiO^- groups. As a result, as deprotonation degree increases, the number of CO_2 molecules in silica nanopores decreases. In addition, as expected, Na^+ ion distributions have a much more prominent peak around the O atom in ≡SiO^- groups than those in ≡SiOH groups due to the net negative charge of ≡SiO^- groups. Cl^- ions enrich at the local minimum of Na^+ ion distributions beyond their peak around the O atom in ≡SiOH groups, while it is depleted from ≡SiO^- groups. The increasing salinity generally lowers the radial densities of water and CO_2 around the O atom in both surface groups.

Fig. 7 presents the water and Na^+ radial distributions around ≡SiOH and ≡SiO^- groups as well as the typical configurations of water molecules and Na^+ ions within a hemi-sphere (radius of 0.6 nm) around the O atom in the surface groups. Fig. 7**(a)** depicts that the hydration structure of water and Na^+ around ≡SiOH groups, where the Ow–Hw bonds of water molecules are pointing toward the O atom in ≡SiOH groups. Na^+ ions are generally depleted from the O atom in ≡SiOH groups as shown in Fig. 7**(c)**. On the other hand, Fig. 7**(b)** illustrates the hydration structure of water and Na^+ around ≡SiO^- groups, in which the peak position of Na^+ is between those of Hw and Ow. Na^+ ions are attracted to the ≡SiO^- groups, especially accumulating in the area where two ≡SiO^- groups are close (see Fig. 7**(d) and 7(e)**). The peak value in Hw distributions is approximately twice of that in Ow distributions, suggesting the Hw–Ow–Hw orientations of water molecules around the ≡SiO^- groups shown in Fig. 7**(d) and 7(e)**.

Fig. 8 presents the radial density distributions of water, CO_2 and salt ions around the O atom in the ≡SiOH and in ≡SiO^- groups, respectively, at various deprotonation degrees. As deprotonation degree increases, water and salt ion radial density profiles around both ≡SiOH and ≡SiO^- groups increase, while those of CO_2 decrease. The increase in water and Cl^- radial density distributions can be partially attributed to the increased number of Na^+ ions close to ≡SiO^- groups. The increases

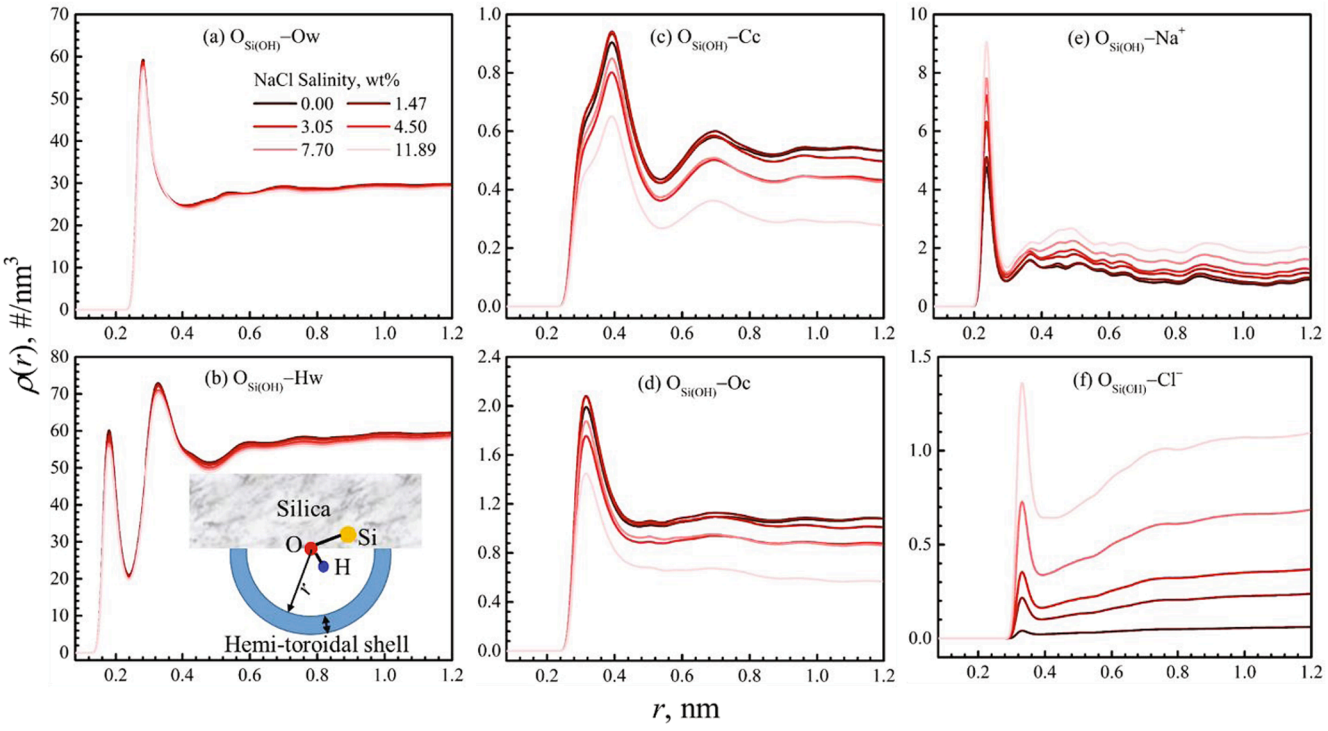

Fig. 5. Radial density distributions of each element around the O atom in ≡SiOH groups at various salinities and deprotonation degree of 16.7%. Ow, Hw, Oc, and Cc represent oxygen and hydrogen atoms of water, oxygen and carbon atoms of CO_2, respectively.

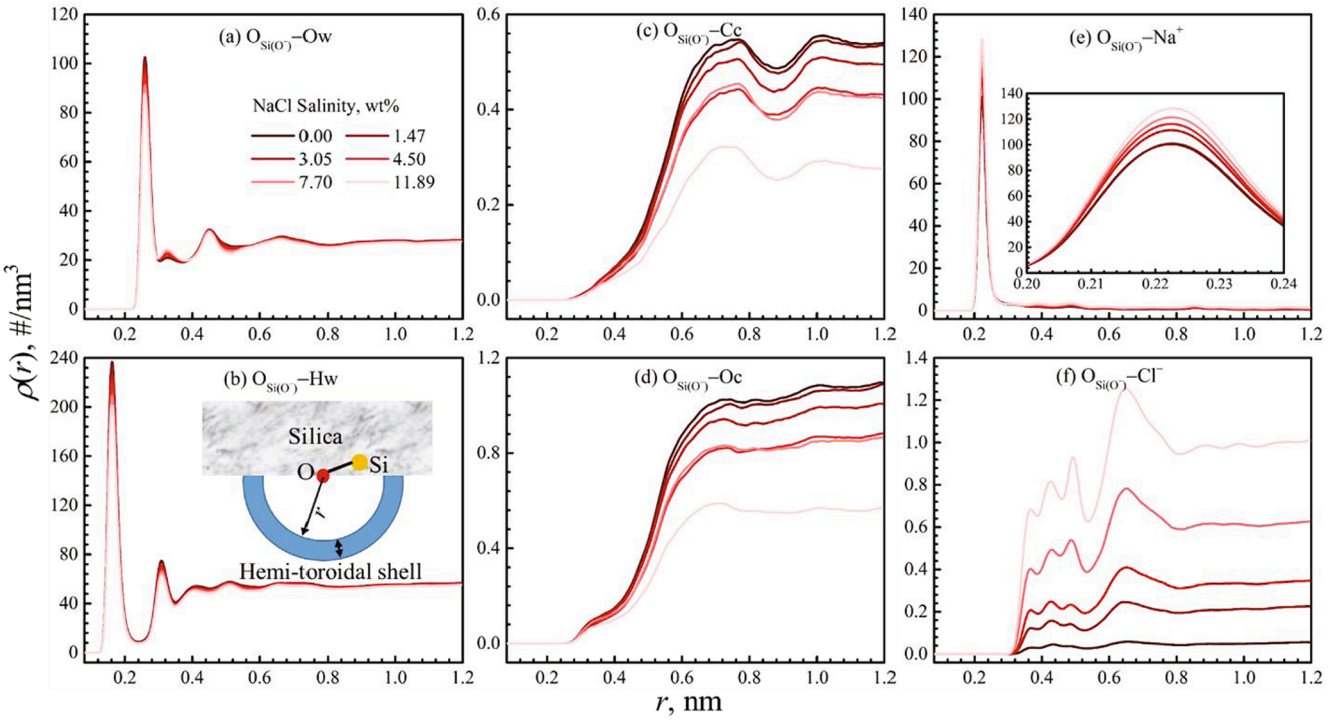

Fig. 6. Radial density distributions of each element around the O atom in ≡SiO^- groups at various salinities and deprotonation degree of 16.7%. Ow, Hw, Oc, and Cc represent oxygen and hydrogen atoms of water, oxygen and carbon atoms of CO_2, respectively.

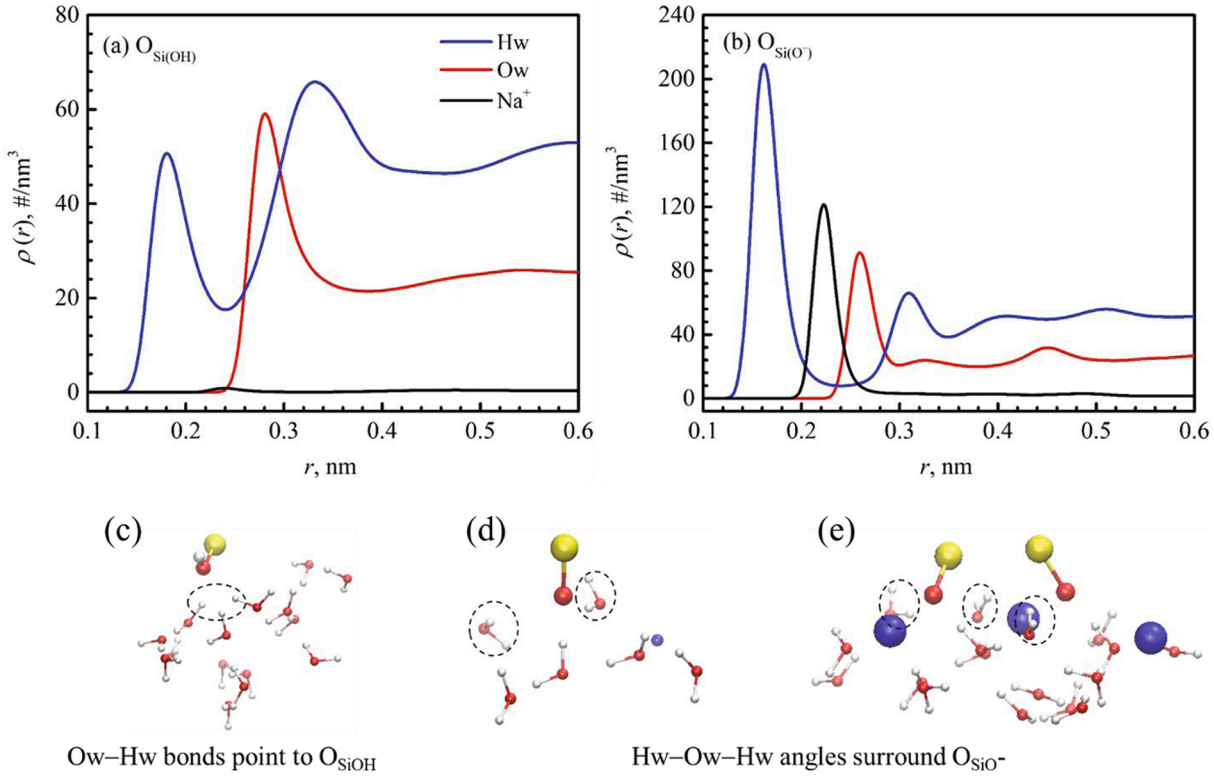

Fig. 7. Radial distribution for Hw (hydrogen of water), Ow (oxygen of water), and Na^+ around the O atom in (a) ≡SiOH groups with deprotonation degree of 0.0% and salinity of 7.33 wt%; (b) ≡SiO^- groups surface deprotonation degree = 16.7% and salinity = 7.70 wt%, respectively. Snapshots of water and Na^+ around (c) ≡SiOH group, (d) ≡SiO^- group at a low local density of ≡SiO^- groups, and (e) ≡SiO^- group at a high local density of ≡SiO^- groups, respectively.

in water and salt ion radial density distributions around ≡SiOH groups are due to an increasing number of ≡SiO^- groups which can greatly attract salt ions and water molecules in their vicinities.

3.4. CO_2 solubility in brine in silica nanopores

CO_2 solubility in brine S in silica nanopores is determined by:

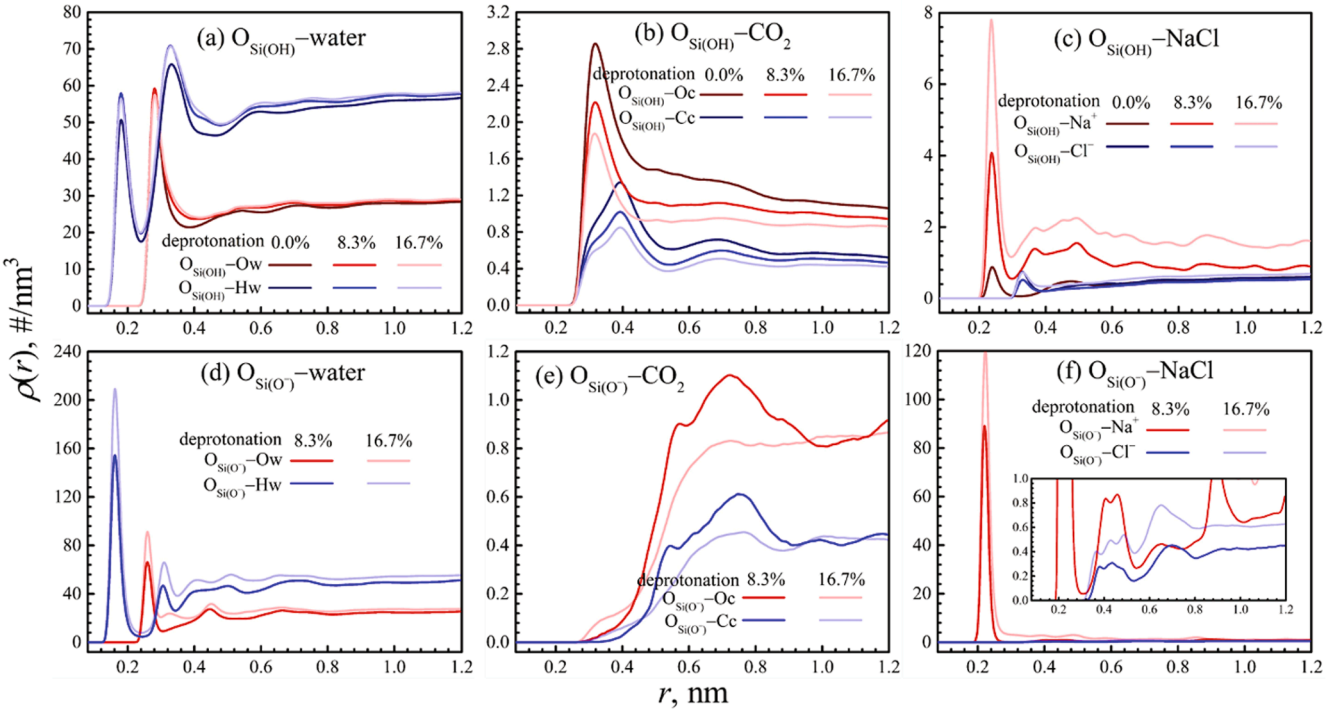

Fig. 8. Radial density distributions of each element around O atom in surface groups under different deprotonation degrees @ salinity = 7.51 ± 0.19 wt%. Ow, Hw, Oc, and Cc represent oxygen and hydrogen atoms of water, oxygen and carbon atoms of CO_2, respectively.

$$S = N_{CO_2}/V_{pore} \quad (2)$$

where N_{CO_2} and V_{pore} are the molar number of CO_2 molecules and the effective pore volume, respectively. The effective pore volume is obtained from helium adsorption by the grand canonical Monte Carlo (GCMC) simulations [37,79,80]. The CO_2 solubility in brine in silica nanopores is presented in Fig. 9.

CO_2 solubility in bulk brine is averaged over all the cases in the outside brine reservoirs (see Fig. 1**(a)**). It is observed that presence of salt ions generally reduces the CO_2 solubility in bulk brine and in brine in silica nanopores. At low pH values (pH values in the ranges of ~2–5 and ~5–7), CO_2 solubility in brine in silica nanopores is generally higher than that in bulk due to the strong CO_2 adsorption on the silica surfaces (see **Figs. 2 and S5**). CO_2 solubility in brine in silica nanopores in the pH range of ~2–5 is 1.3–1.6 times of that in bulk. As pH further increases (pH values in the range of ~7–9), CO_2 solubility in brine in silica nanopores becomes comparable to that in bulk brine. Collectively, low salinity and low pH conditions are favorable for CO_2 storage by solubility trapping in silica nanopores in tight formations. We note that in our previous work [37], CO_2 solubility in water is reduced in kaolinite nanopores with gibbsite facet as inner-surface (strong hydrophilic), while enhanced in kaolinite nanopores with silica facet as inner-surface (less hydrophilic). The results in this work are consistent with our previous one [37] as silica surface becomes more hydrophilic as its surface deprotonation degree increases [17].

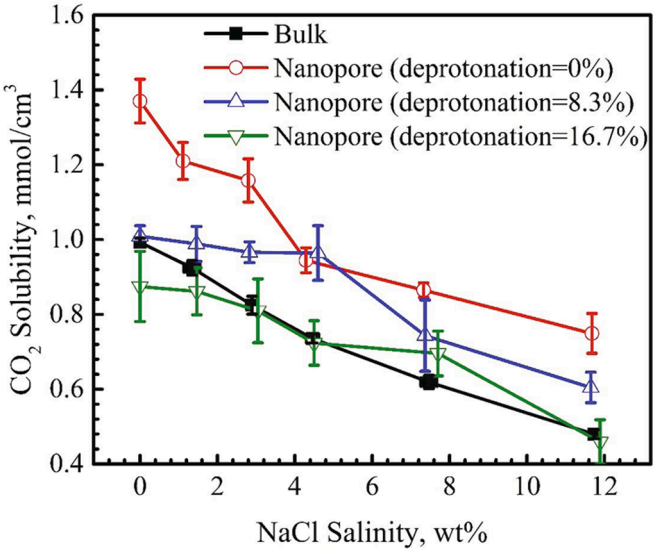

Fig. 9. CO_2 solubility in brine in silica nanopores under various conditions. For comparison, we also present CO_2 solubility in bulk brine.

4. Conclusion

In this work, MD simulation is used to study the coordinated effect of pH and salinity on the fluid distributions and CO_2 solubility in brine in silica nanopores, which have been poorly understood but can be of practical significance for geological CO_2 sequestration in tight formations. The number density distributions normal to the silica surface, 2-D density contour plots parallel to the surface, and radial distributions around the surface groups are presented to obtain a comprehensive understanding of fluid structural properties under various conditions.

In non-deprotonated cases, water has a layered structure close to the silica surface, and CO_2 molecules co-adsorb on the silica surface with water, while ions are depleted from the silica surface. As deprotonation degree gradually increases (from 0% to 16.7%), water adsorption becomes increasingly significant and CO_2 adsorption gradually decreases, while Na^+ ions are strongly attracted by the silica surface, forming several density spikes. The 2-D density contour plots reveal that water molecules enrich around the surface groups on the surface, while CO_2 molecules accumulate in the areas away from the surface groups. Na^+ ions are strongly attracted to the deprotonated surface groups. The water orientation around ≡SiOH and ≡SiO^- groups are different due to the different water hydration structures. The radial distributions of CO_2

have a peak around the ≡SiOH groups, while they are generally depleted from the ≡SiO^- groups. Overall, the increase in salinity generally lowers both water and CO_2 density distributions in silica nanopores. Collectively, CO_2 solubility in brine in silica nanopores decreases as salinity and pH increases, and CO_2 solubility in brine in silica nanopores can be 30–60% higher than that in bulk for low pH cases in the salinity range of 0–12 wt%. Therefore, low salinity and low pH environments are favored for geological CO_2 sequestration by solubility trapping in silica nanopores in tight formations. Considering that in tight formations, there are a large number of nanoscale pores, CO_2 dissolution in brine in silica nanopores may play an important role in CO_2 sequestration during CO_2-EOR in tight formations. Our work provides some important insights into the CO_2 sequestration during CO_2-EOR in tight formations and the optimization of the process.

The dissolved CO_2 in brine is subject to the reaction with water to form carbonic acid, which is a weak acid. The pH value of CO_2 saturated water solution is ~3.2 under the conditions in this work according to experimental measurements [81]. This suggests that the pH of brine decreases as CO_2 dissolves into the brine. The acidic environment is beneficial for CO_2 solubility in brine in silica nanopores, but this process (CO_2 dissolution in brine in silica nanopores and silica surface chemistry alteration) might take a long time, especially in tight formations. However, the solubility trapping mechanism has the time scale of thousands of years [1] and the dissolved CO_2 in brine in silica nanopores can incur the subsequent mineral trapping [82]. On the other hand, the findings in this work are only applicable for an equilibrium system, while the dynamic properties (e.g., the process of CO_2 dissolving into brine by advection or diffusion) are not discussed, which are also important to the CCS procedures. In our future work, we would explicitly explore the dynamic process of geological CO_2 sequestration.

Declaration of Competing Interest

The authors declare that they have no known competing financial interests or personal relationships that could have appeared to influence the work reported in this paper.

Acknowledgments

The authors acknowledge the China Scholarship Council (CSC) for the financial support provided to W. Li. This research was enabled in part by support provided by Westgrid (www.westgrid.ca) and Compute Canada (www.computecanada.ca). The authors also greatly acknowledge a Discovery Grant from Natural Sciences and Engineering Research Council of Canada (NSERC RGPIN-2017-05080) and National Natural Science Foundation of China (51874261).

Appendix A. Supplementary data

Supplementary data to this article can be found online at https://doi.org/10.1016/j.cej.2020.127626.

References

[1] M. Bui, C.S. Adjiman, A. Bardow, E.J. Anthony, A. Boston, S. Brown, P.S. Fennell, S. Fuss, A. Galindo, L.A. Hackett, J.P. Hallett, H.J. Herzog, G. Jackson, J. Kemper, S. Krevor, G.C. Maitland, M. Matuszewski, I.S. Metcalfe, C. Petit, G. Puxty, J. Reimer, D.M. Reiner, E.S. Rubin, S.A. Scott, N. Shah, B. Smit, J.P.M. Trusler, P. Webley, J. Wilcox, N. Mac Dowell, Carbon capture and storage (CCS): the way forward, Energy Environ. Sci. 11 (2018) 1062–1176.

[2] M.A. Celia, S. Bachu, J. Nordbotten, K. Bandilla, Status of CO2 storage in deep saline aquifers with emphasis on modeling approaches and practical simulations, Water Resour. Res. 51 (2015) 6846–6892.

[3] K. Michael, A. Golab, V. Shulakova, J. Ennis-King, G. Allinson, S. Sharma, T. Aiken, Geological storage of CO2 in saline aquifers—A review of the experience from existing storage operations, Int. J. Greenhouse Gas Control 4 (2010) 659–667.

[4] A. Hosa, M. Esentia, J. Stewart, S. Haszeldine, Injection of CO2 into saline formations: Benchmarking worldwide projects, Chem. Eng. Res. Des. 89 (2011) 1855–1864.

[5] J.K. Eccles, L. Pratson, R.G. Newell, R.B. Jackson, Physical and economic potential of geological CO2 storage in saline aquifers, Environ. Sci. Technol. 43 (2009) 1962–1969.

[6] Global CCS Institute, The global status of CCS: 2019. Targeting Climate Change, (2019).

[7] US Energy Information Administration, Annual Energy Outlook 2019, (2019).

[8] X. Zhang, B. Wei, J. Shang, K. Gao, W. Pu, X. Xu, C. Wood, L. Sun, Alterations of geochemical properties of a tight sandstone reservoir caused by supercritical CO2-brine-rock interactions in CO2-EOR and geosequestration, J. CO2 Util. 28 (2018) 408–418.

[9] Z. Song, Y. Song, Y. Li, B. Bai, K. Song, J. Hou, A critical review of CO2 enhanced oil recovery in tight oil reservoirs of North America and China, Fuel 276 (2020), 118006.

[10] W. Pu, B. Wei, F. Jin, Y. Li, H. Jia, P. Liu, Z. Tang, Experimental investigation of CO2 huff-n-puff process for enhancing oil recovery in tight reservoirs, Chem. Eng. Res. Des. 111 (2016) 269–276.

[11] B. Jia, J.-S. Tsau, R. Barati, A review of the current progress of CO2 injection EOR and carbon storage in shale oil reservoirs, Fuel 236 (2019) 404–427.

[12] R.D. Thomas, D.C. Ward, Effect of overburden pressure and water saturation on gas permeability of tight sandstone cores, J. Petrol. Technol. 24 (1972) 120–124.

[13] W. Tian, A. Li, X. Ren, Y. Josephine, The threshold pressure gradient effect in the tight sandstone gas reservoirs with high water saturation, Fuel 226 (2018) 221–229.

[14] R.C. Selley, S.A. Sonnenberg, Elements of petroleum geology, Gulf Professional Publishing, 2015.

[15] C. Lyu, Z. Ning, Q. Wang, M. Chen, Application of NMR T 2 to pore size distribution and movable fluid distribution in tight sandstones, Energy Fuels 32 (2018) 1395–1405.

[16] F. Wang, K. Yang, J. You, X. Lei, Analysis of pore size distribution and fractal dimension in tight sandstone with mercury intrusion porosimetry, Results Phys. 13 (2019), 102283.

[17] C. Chen, N. Zhang, W. Li, Y. Song, Water contact angle dependence with hydroxyl functional groups on silica surfaces under CO2 sequestration conditions, Environ. Sci. Technol. 49 (2015) 14680–14687.

[18] A. Luzar, D. Bratko, Gas solubility in hydrophobic confinement, J. Phys. Chem. B 109 (2005) 22545–22552.

[19] D. Bratko, A. Luzar, Attractive surface force in the presence of dissolved gas: A molecular approach, Langmuir 24 (2008) 1247–1253.

[20] Y. Qiao, G. Cao, X. Chen, Effects of gas molecules on nanofluidic behaviors, J. Am. Chem. Soc. 129 (2007) 2355–2359.

[21] S. Miachon, V.V. Syakaev, A. Rakhmatullin, M. Pera-Titus, S. Caldarelli, J. A. Dalmon, Higher gas solubility in nanoliquids? ChemPhysChem 9 (2008) 78–82.

[22] M. Pera-Titus, S. Miachon, J.A. Dalmon, Increased gas solubility in nanoliquids: Improved performance in interfacial catalytic membrane contactors, AIChE J. 55 (2009) 434–441.

[23] V. Rakotovao, R. Ammar, S. Miachon, M. Pera-Titus, Influence of the mesoconfining solid on gas oversolubility in nanoliquids, Chem. Phys. Lett. 485 (2010) 299–303.

[24] A. Botan, B. Rotenberg, V. Marry, P. Turq, B. Noetinger, Carbon Dioxide in Montmorillonite Clay Hydrates: Thermodynamics, Structure, and Transport from Molecular Simulation, J. Phys. Chem. C 114 (2010) 14962–14969.

[25] N.L. Ho, F. Porcheron, R.-J.-M. Pellenq, Experimental and molecular simulation investigation of enhanced CO2 solubility in hybrid adsorbents, Langmuir 26 (2010) 13287–13296.

[26] L.N. Ho, J. Perez Pellitero, F. Porcheron, R.-J.-M. Pellenq, Enhanced CO2 solubility in hybrid MCM-41: molecular simulations and experiments, Langmuir 27 (2011) 8187–8197.

[27] N.L. Ho, J. Perez-Pellitero, F. Porcheron, R.-J.-M. Pellenq, Enhanced CO2 solubility in hybrid adsorbents: optimization of solid support and solvent properties for CO2 capture, J. Phys. Chem. C 116 (2012) 3600–3607.

[28] S. Clauzier, L.N. Ho, M. Pera-Titus, B. Coasne, D. Farrusseng, Enhanced H2 uptake in solvents confined in mesoporous metal–organic framework, J. Am. Chem. Soc. 134 (2012) 17369–17371.

[29] E. Soubeyrand-Lenoir, C. Vagner, J.W. Yoon, P. Bazin, F. Ragon, Y.K. Hwang, C. Serre, J.-S. Chang, P.L. Llewellyn, How water fosters a remarkable 5-fold increase in low-pressure CO2 uptake within mesoporous MIL-100 (Fe), J. Am. Chem. Soc. 134 (2012) 10174–10181.

[30] L.N. Ho, S.p. Clauzier, Y. Schuurman, D. Farrusseng, B. Coasne, Gas uptake in solvents confined in mesopores: adsorption versus enhanced solubility, J. Phys. Chem. Lett. 4 (2013) 2274–2278.

[31] A. Phan, D.R. Cole, A. Striolo, Aqueous methane in slit-shaped silica nanopores: high solubility and traces of hydrates, J. Phys. Chem. C 118 (2014) 4860–4868.

[32] L.N. Ho, Y. Schuurman, D. Farrusseng, B. Coasne, Solubility of gases in water confined in nanoporous materials: ZSM-5, MCM-41, and MIL-100, J. Phys. Chem. C 119 (2015) 21547–21554.

[33] Y. Hu, L. Huang, S. Zhao, H. Liu, K.E. Gubbins, Effect of confinement in nanoporous materials on the solubility of a supercritical gas, Mol. Phys. 114 (2016) 3294–3306.

[34] G. Gadikota, B. Dazas, G. Rother, M.C. Cheshire, I.C. Bourg, Hydrophobic solvation of gases (CO2, CH4, H2, noble gases) in clay interlayer nanopores, J. Phys. Chem. C 121 (2017) 26539–26550.

[35] S.B. Badmos, A. Striolo, D.R. Cole, Aqueous Hydrogen Sulfide in Slit-Shaped Silica Nanopores: Confinement Effects on Solubility, Structural, and Dynamical Properties, J. Phys. Chem. C 122 (2018) 14744–14755.

[36] B. Coasne, D. Farrusseng, Gas oversolubility in nanoconfined liquids: Review and perspectives for adsorbent design, Microporous Mesoporous Mater. 288 (2019), 109561.
[37] W. Li, Y. Nan, Z. Zhang, Q. You, Z. Jin, Hydrophilicity/Hydrophobicity Driven CO2 Solubility in Kaolinite Nanopores in Relation to Carbon Sequestration, Chem. Eng. J. 398 (2020), 125449.
[38] C. Qiao, X. Yu, X. Song, T. Zhao, X. Xu, S. Zhao, K.E. Gubbins, Enhancing Gas Solubility in Nanopores: A Combined Study Using Classical Density Functional Theory and Machine Learning, Langmuir 36 (2020) 8527–8536.
[39] J. Hu, Z. Duan, C. Zhu, I.-M. Chou, PVTx properties of the CO2–H2O and CO2–H2O–NaCl systems below 647 K: Assessment of experimental data and thermodynamic models, Chem. Geol. 238 (2007) 249–267.
[40] Z. Duan, R. Sun, An improved model calculating CO2 solubility in pure water and aqueous NaCl solutions from 273 to 533 K and from 0 to 2000 bar, Chem. Geol. 193 (2003) 257-271.
[41] W. Yan, S. Huang, E.H. Stenby, Measurement and modeling of CO2 solubility in NaCl brine and CO2–saturated NaCl brine density, Int. J. Greenhouse Gas Control 5 (2011) 1460–1477.
[42] N. Spycher, K. Pruess, CO2-H2O Mixtures in the Geological Sequestration of CO2. II. Partitioning in Chloride Brines at 12–100 C and up to 600 bar, Geochim. Cosmochim. Acta 69 (2005) 3309–3320.
[43] A. Malani, K. Ayappa, S. Murad, Effect of confinement on the hydration and solubility of NaCl in water, Chem. Phys. Lett. 431 (2006) 88–93.
[44] F.S. Emami, V. Puddu, R.J. Berry, V. Varshney, S.V. Patwardhan, C.C. Perry, H. Heinz, Force field and a surface model database for silica to simulate interfacial properties in atomic resolution, Chem. Mater. 26 (2014) 2647–2658.
[45] Y. Duval, J. Mielczarski, O. Pokrovsky, E. Mielczarski, J. Ehrhardt, Evidence of the existence of three types of species at the quartz− aqueous solution interface at pH 0–10: XPS surface group quantification and surface complexation modeling, J. Phys. Chem. B 106 (2002) 2937–2945.
[46] I.C. Bourg, C.I. Steefel, Molecular dynamics simulations of water structure and diffusion in silica nanopores, J. Phys. Chem. C 116 (2012) 11556–11564.
[47] M. Collin, S. Gin, B. Dazas, T. Mahadevan, J. Du, I.C. Bourg, Molecular dynamics simulations of water structure and diffusion in a 1 nm diameter silica nanopore as a function of surface charge and alkali metal counterion identity, J. Phys. Chem. C 122 (2018) 17764–17776.
[48] P.A. Bonnaud, B. Coasne, R.J.-M. Pellenq, Solvated calcium ions in charged silica nanopores, J. Chem. Phys. 137 (2012), 064706.
[49] R. Renou, A. Szymczyk, A. Ghoufi, Water confinement in nanoporous silica materials, J. Chem. Phys. 140 (2014), 044704.
[50] N.R. Haria, C.D. Lorenz, Ion exclusion and electrokinetic effects resulting from electro-osmotic flow of salt solutions in charged silica nanopores, PCCP 14 (2012) 5935–5944.
[51] N.R. Haria, C.D. Lorenz, Atomistic description of pressure-driven flow of aqueous salt solutions through charged silica nanopores, J. Phys. Chem. C 119 (2015) 12298–12311.
[52] D. Frenkel, B. Smit, Understanding molecular simulation: from algorithms to applications, Elsevier, 2001.
[53] A. Almeida da Costa, P. Jaeger, J. Santos, J. Soares, M. Embiruçu, G. Meyberg, The Influence of Rock Composition and pH on Reservoir Wettability for Low Salinity Water-CO EOR Applications in Brazilian Reservoirs, SPE Annual Technical Conference and Exhibition, Soc. Petrol. Eng. (2019).
[54] C. Hu, Y. Zhang, Z. Yang, Z. Zhang, H. Fan, Q. You, Experimental study on functional characteristics of pH-sensitive nanoparticles for pressure reduction and augmented injection in tight oil reservoir, J. Mol. Liq. 113253 (2020).
[55] A.L. Soli, R.H. Byrne, CO2 system hydration and dehydration kinetics and the equilibrium CO2/H2CO3 ratio in aqueous NaCl solution, Mar. Chem. 78 (2002) 65–73.
[56] L. Zhuravlev, Characterization of amorphous silica surface, React. Kinet. Catal. Lett. 50 (1993) 15–25.
[57] L. Zhuravlev, The surface chemistry of amorphous silica. Zhuravlev model, Colloid. Surf. A Physicochem. Eng. Aspects 173 (2000) 1–38.
[58] S.M. Chemtob, G.R. Rossman, J.F. Stebbins, Natural hydrous amorphous silica: Quantitation of network speciation and hydroxyl content by 29Si MAS NMR and vibrational spectroscopy, Am. Mineral. 97 (2012) 203–211.
[59] H. Berendsen, J. Grigera, T. Straatsma, The missing term in effective pair potentials, J. Phys. Chem. 91 (1987) 6269–6271.
[60] J.G. Harris, K.H. Yung, Carbon dioxide's liquid-vapor coexistence curve and critical properties as predicted by a simple molecular model, J. Phys. Chem. 99 (1995) 12021–12024.
[61] D.E. Smith, L.X. Dang, Computer simulations of NaCl association in polarizable water, J. Chem. Phys. 100 (1994) 3757–3766.
[62] E. Lemmon, M. McLinden, D. Friend, P. Linstrom, W. Mallard, NIST chemistry WebBook, Nist standard reference database number 69, National Institute of Standards and Technology, Gaithersburg, https://doi.org/10.18434/T4D303, (retrieved April 18, 2020) (2020).
[63] L.M. Pereira, A. Chapoy, R. Burgass, M.B. Oliveira, J.A. Coutinho, B. Tohidi, Study of the impact of high temperatures and pressures on the equilibrium densities and interfacial tension of the carbon dioxide/water system, J. Chem. Thermodyn. 93 (2016) 404–415.
[64] S.P. Cadogan, G.C. Maitland, J.M. Trusler, Diffusion coefficients of CO2 and N2 in water at temperatures between 298.15 K and 423.15 K at pressures up to 45 MPa, J. Chem. Eng. Data 59 (2014) 519–525.
[65] L. Vlcek, A.A. Chialvo, D.R. Cole, Optimized unlike-pair interactions for water–carbon dioxide mixtures described by the SPC/E and EPM2 models, J. Phys. Chem. B 115 (2011) 8775–8784.
[66] J. Kolafa, Solubility of NaCl in water and its melting point by molecular dynamics in the slab geometry and a new BK3-compatible force field, J. Chem. Phys. 145 (2016), 204509.
[67] J. Espinosa, J. Young, H. Jiang, D. Gupta, C. Vega, E. Sanz, P.G. Debenedetti, A. Z. Panagiotopoulos, On the calculation of solubilities via direct coexistence simulations: Investigation of NaCl aqueous solutions and Lennard-Jones binary mixtures, J. Chem. Phys. 145 (2016), 154111.
[68] A. Benavides, J. Aragones, C. Vega, Consensus on the solubility of NaCl in water from computer simulations using the chemical potential route, J. Chem. Phys. 144 (2016), 124504.
[69] I. Zeron, J. Abascal, C. Vega, A force field of Li+, Na+, K+, Mg2+, Ca2+, Cl−, and SO 4 2− in aqueous solution based on the TIP4P/2005 water model and scaled charges for the ions, J. Chem. Phys. 151 (2019), 134504.
[70] C. Chalbaud, M. Robin, J. Lombard, F. Martin, P. Egermann, H. Bertin, Interfacial tension measurements and wettability evaluation for geological CO2 storage, Adv. Water Resour. 32 (2009) 98–109.
[71] H.J. Berendsen, D. van der Spoel, R. van Drunen, GROMACS: a message-passing parallel molecular dynamics implementation, Comput. Phys. Commun. 91 (1995) 43–56.
[72] D. Van Der Spoel, E. Lindahl, B. Hess, G. Groenhof, A.E. Mark, H.J. Berendsen, GROMACS: fast, flexible, and free, J. Comput. Chem. 26 (2005) 1701–1718.
[73] M. Allen, D.J. Tildesley, Computer simulation of liquids, Clarendon Press, Oxford, 1987.
[74] U. Essmann, L. Perera, M.L. Berkowitz, T. Darden, H. Lee, L.G. Pedersen, A smooth particle mesh Ewald method, J. Chem. Phys. 103 (1995) 8577–8593.
[75] S. Miyamoto, P.A. Kollman, Settle: An analytical version of the SHAKE and RATTLE algorithm for rigid water models, J. Comput. Chem. 13 (1992) 952–962.
[76] H. Berendsen, W. Van Gunsteren, Molecular dynamics simulations: Techniques and approaches, Molecular Liquids, Springer, 1984, pp. 475–500.
[77] G. Bussi, D. Donadio, M. Parrinello, Canonical sampling through velocity rescaling, J. Chem. Phys. 126 (2007), 014101.
[78] W. Humphrey, A. Dalke, K. Schulten, VMD: visual molecular dynamics, J. Mol. Graph. 14 (1996) 33–38.
[79] W. Pang, Y. He, C. Yan, Z. Jin, Tackling the challenges in the estimation of methane absolute adsorption in kerogen nanoporous media from molecular and analytical approaches, Fuel 242 (2019) 687–698.
[80] Y. Tian, C. Yan, Z. Jin, Characterization of methane excess and absolute adsorption in various clay nanopores from molecular simulation, Sci. Rep. 7 (2017) 12040.
[81] C. Peng, J.P. Crawshaw, G.C. Maitland, J.M. Trusler, D. Vega-Maza, The pH of CO2-saturated water at temperatures between 308 K and 423 K at pressures up to 15 MPa, J. Supercrit. Fluids 82 (2013) 129–137.
[82] B. Smit, J.A. Reimer, C.M. Oldenburg, I.C. Bourg, Introduction to carbon capture and sequestration, World Scientific, 2014.